Coastal Dynamics 2017
Paper No. 041

INFRAGRAVITY WAVE DYNAMICS ON AN EMBAYED BEACH

Diogo Mendes[123], José P. Pinto[2], António A. Pires-Silva[1] and André B. Fortunato[3]

Abstract

Field observations were performed at an embayed beach to investigate infragravity (IG) wave (0.005-0.04 Hz) dynamics. Offshore short-wave conditions measured by the Cabo Sillero buoy (323 m depth) were characterized by a mean significant wave height of 0.9 m and a mean peak wave period of 9 s. Analysis of field observations demonstrate that for this embayed beach two IG wave peaks can be detected (0.01 and 0.025 Hz). The IG wave band can be separated in two frequency bands due to the different wave propagation characteristics (0.005-0.02 and 0.02-0.04 Hz). The bound wave generation mechanism was identified based on a negative correlation between the short-wave envelope and the IG wave elevation for a time lag of 5 s. The phase-lag evolution of the IG wave increasingly lags behind the short-wave envelope shorewards.

Keywords: bound wave, phase-lag evolution, field measurements, cross-spectral analysis

1. Introduction

Infragravity (IG) waves are low-frequency surface waves with periods between 25 and 250 s. Their role in the coastal zone has long been recognized because IG waves may be responsible for beach erosion (Russel, 1993) and they can explain the formation of many morphological features (e.g. Aagaard, 1990). Moreover, they also play a role in harbors and marinas which are designed to avoid the amplification of IG waves due to the resonance phenomenon (Rabinovich, 2008).

Two widely accepted mechanisms were proposed for the generation of IG waves. The first was proposed by Longuet-Higgins and Stewart (1962) and is due to the higher radiation stresses below the crests of the short wave (SW) groups that induce an IG wave bound to the SW group. According to this theory, the IG bound wave is 180º out of phase with the SW group. The second generation mechanism is related to the shifting of the breakpoint position (Symonds *et al*., 1982). The breakpoint displacement induces a time-varying set-up/down which results in an IG wave that propagates both seaward and shoreward from the breaking point. The dominant IG wave generation mechanism seems to depend on the beach slope (Battjes *et al.*, 2004) and short wave steepness (Baldock and Huntley, 2002).

Masselink (1995) and Inch *et al.* (2017) identified IG bound wave evidence based on field measurements. These authors have found that the IG bound wave lags between 4 to 7 s from the SW envelope and, according to Janssen *et al.* (2003), this seems to be a condition for the energy to be transferred from SW to the IG bound waves. De Bakker *et al.* (2013) presented results of the phase-lag evolution of the IG wave behind the SW envelope. The phase-lag was frequency-dependent and grew from 0, at offshore, up to 1.5 π at the SW breaking point.

Most of the above mentioned field studies were carried out in open-beaches, which differ significantly from embayed beaches. These beaches are delimited by two natural or artificial promontories (Short and Masselink, 1999). Several studies on embayed beaches have addressed extensively the morphodynamics with time-scales ranging from storm-events to decades (e.g. Loureiro et al., 2012; Castelle and Coco, 2012) and the rip systems (e.g. MacMahan et al., 2006). IG waves were also found to contribute for a substantial part of a rip current system (up to 50 %) that eventually is formed (MacMahan et al., 2006). Nevertheless, the general IG wave dynamic patterns, such as generation, propagation and dissipation, were usually not

[1]CERIS, Instituto Superior Técnico, Universidade de Lisboa, Lisbon, Portugal. ddiogosm@gmail.com
[2]Instituto Hidrográfico, Lisbon, Portugal.
[3]Laboratório Nacional de Engenharia Civil, Lisbon, Portugal.

tackled in those studies.

Despite the importance of IG waves and embayed beaches in coastal areas, and to our best knowledge, there is no evidence of a study that links both. Here, we propose to investigate the IG wave dynamics on an embayed beach based on field measurements. Topics that are going to be considered are propagation, generation and phase-lag evolution regarding IG waves. This way the comprehension of IG dynamics on embayed beaches is extended.

2. Methodology

2.1. *Field site and data collection*

Field data were collected from 30 September to 1 October 2015 during spring tides at the Vila Praia de Âncora beach, Portugal (Figure 1 – a) and b)). The Vila Praia de Âncora beach experiences a mesotidal regime with a mean tidal range of 3 m and is limited by two rocky promontories.

The beach faces west northwest and is exposed to both Atlantic swells and locally generated wind waves. The cross-shore profile is characterized by a dissipative profile (1:70) up to the mean sea level (MSL) position, when it suddenly steepens to a slope of approximately 1:20. The beach is composed of medium sand (D_{50} = 0.5 mm).

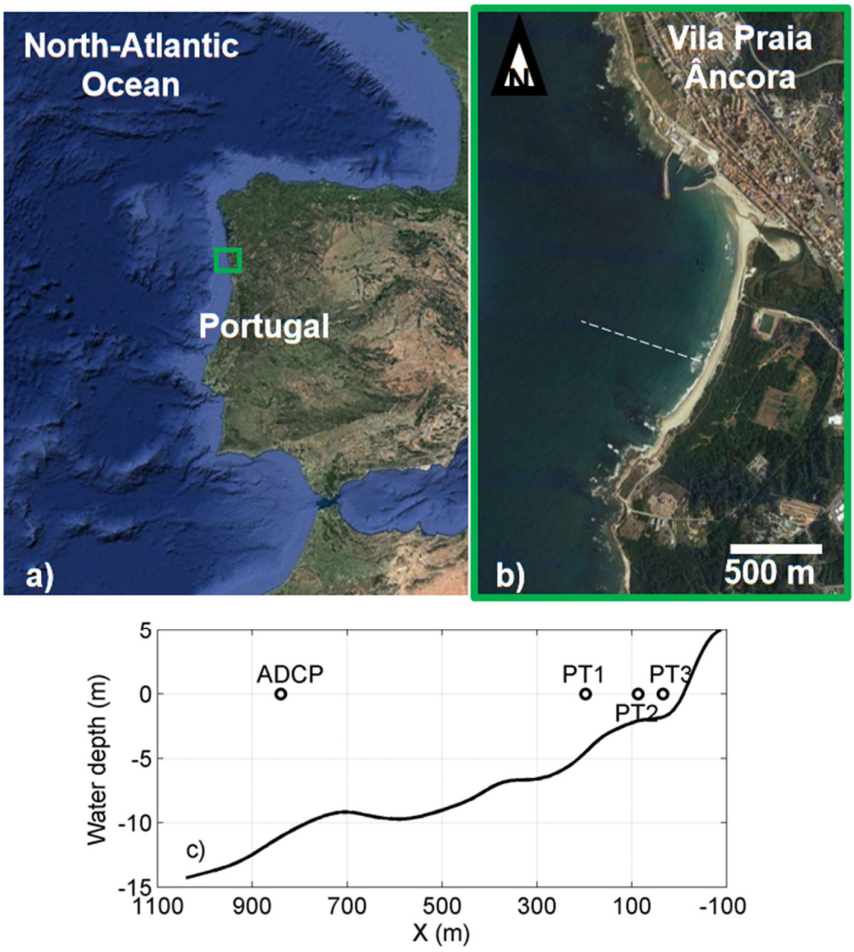

Figure 1 – Geographic location of the Vila Praia de Âncora beach (a) and b), adapted from GoogleEarth). Topo-bathymetric profile based on the 2011 LIDAR information and instruments positions (c)). Water depth is relative to mean sea level.

Pressure observations were recorded continuously at 2 Hz by three synchronized pressure transducers (PT) (Figure 1c)). The PT3 was deployed near the intertidal zone and it was attached to a spider-like structure that allowed us to record the pressure fluctuations in very shallow waters during low-tide. PT2, PT3 and the acoustic Dopler current profiler (ADCP) were moored in the subtidal zone using a boat.

The bathymetric survey was not performed during the field experiment and the 2011 LIDAR topo-bathymetric information will be used. The intertidal zone was surveyed using a quad-bike. Offshore SW conditions measured by the Cabo Sillero buoy (323 m depth) were characterized by a mean significant SW height of 0.9 m and a mean peak wave period of 9 s. The wave conditions measured by the ADCP were characterized by a mean significant SW height of 0.7 m, a mean peak period of 10 s and a mean wave direction 20º south from shore normal. Spring tidal amplitudes varied between -1.6 and 1.8 m relative to MSL.

2.2. *Data processing and analysis*

The pressure data were corrected from atmospheric pressure, converted to water depth assuming a vertical hydrostatic pressure balance and filtered using a 3rd-order Butterworth filter in order to separate three different signals. The tidal signal was obtained with a low-pass filter with a 0.005 Hz cut-off frequency, the IG signal was band-passed between 0.005-0.04 Hz and the SW signal was band-passed between 0.04-0.33 Hz.

These limits are consistent with several studies on unlimited fetch beaches (e.g. Inch et al., 2017). Following Janssen et al. (2003), the low-frequency fluctuations associated with the wave groups were computed using a SW envelope concept.. The envelope is based on the Hilbert transform:

$$A(t) = |\eta^{sw} + i\Gamma\{\eta^{sw}\}|_{IG} \quad (1)$$

where $\Gamma\{\}$ denotes the Hilbert transform operator, η is the sea-surface elevation and SW and IG stands for band-pass filtering within the previous mentioned frequencies. The significant wave height for the IG (Hm_0^{IG}) and SW (Hm_0^{SW}) bands were calculated as four times the standard deviation of the sea-surface elevation time series. Here, 40 min time series centered either at low or high tides were used to ensure that stationary conditions are met and to guarantee an adequate statistical significance for the auto-spectral, cross-spectral and cross-correlation estimates. The mean water depth was defined as the mean value of the tidal signal for each 40 min.

Auto-spectra were computed dividing the signal in 8 Hanning-tappered and 50% overlapped blocks of 1024 samples (~ 38 min). This procedure gave a frequency resolution of 0.002 Hz with 14 degrees of freedom (dof). Cross-spectra were calculated in a similar way. The squared coherence 95% confidence interval was calculated based on the dof and this yielded a value of 0.35. Cross-correlation was also computed between two dependent correlated signals using 4096 samples (N) following Masselink (1995). The reduced number of independent samples (N*) was calculated using the expression of Garret and Petrie (1981):

$$N^{*-1} = N^{-1} + 2N^{-2}\sum_{j=1}^{N-1}(N-j)R_{xy}(j\tau) \quad (2)$$

where R_{xy} is the auto-correlation function. The corresponding 95% confidence limits for the auto-correlation function was estimated as:

$$1.96/\sqrt{N^*} \quad (3)$$

3. Results and discussion

3.1. *Wave statistics*

Table 1 presents the hydrodynamic conditions during each tidal cycle of the field experiment. During low-tides (TIDE 1 and 3), Hm_0^{SW} increased between the ADCP and the PT1 and then decreased shorewards at PT2 and PT3. This behavior is representative of shoaling and further breaking wave conditions. Since no video-camera was available, the definition of the water depth at the breaking position cannot be accurately

determined. Therefore, we assumed a wave height to water depth ratio (γ_b) of 0.33. This value was found by Ruessink (1998) on a multiple-barred dissipative profile with a slope of 1:100. It was hereafter assumed that wave breaking took place between PT1 and PT2 during low-tides and this is, in fact, in accordance with visual observations during the field experiment.

It was also assumed that during high-tides all the sensors were located seaward from the breaking zone. The ratio between IG and SW Hm0 was around 10% during high-tides. During low-tides, this value increased from 10% up to around 60% for the shallowest sensor (PT3). Even under low-energy conditions, IG waves contribute that much to wave energy near the shore, consistent with previous studies (e.g. Guza and Thornton, 1985).

Since the offshore wave forcing and tidal levels were similar when comparing both low- or high-tides, further analysis in this study will regard only the comparison between TIDE 1 and TIDE 2. The SW (thin lines) and IG (thick lines) sea-surface elevations and the SW envelope (dashed lines) time-series for 500 s around the mean water depth are compared in Figure 2. During low-tide (Figure 2a)), the IG sea-surface elevation at PT1 was consistent with the bound wave theory due to the phase lag of 180º from the SW wave envelope. At PT2, the wave groups were already destroyed due to depth-induced breaking, in accordance with the assumption made regarding the location of each instrument, and this reduced the fluctuations of the SW envelope. Further onshore the IG elevation seems to dominate the fluctuations.

During high-tide the behavior was different since the three PTs were located offshore of the breaking position. Actually, the phase lag of 180º was not so evident probably because of both the deeper water depth and the low-energetic SW conditions experienced during the field campaign.

Table 1 – Short and infragravity wave parameters for each low- and high-tide observed during the field experiment.

TIDE 1 (low-tide)					
PT No.	**h (m)**	**Hm_0^{IG} (m)**	**Hm_0^{SW} (m)**	**Hm_0^{IG}/Hm_0^{SW}**	**Hm_0^{SW}/h**
3	0.42	0.13	0.21	0.63	0.34
2	2.20	0.13	0.37	0.35	0.17
1	3.30	0.13	0.82	0.16	0.24
ADCP	11.5	-	0.67	-	-
TIDE 2 (high-tide)					
PT No.	**h (m)**	**Hm_0^{IG} (m)**	**Hm_0^{SW} (m)**	**Hm_0^{IG}/Hm_0^{SW}**	**Hm_0^{SW}/h**
3	3.95	0.11	0.80	0.14	0.22
2	5.61	0.09	0.67	0.13	0.12
1	6.88	0.08	0.79	0.11	0.12
ADCP	15.1	-	0.75	-	-
TIDE 3 (low-tide)					
PT No.	**h (m)**	**Hm_0^{IG} (m)**	**Hm_0^{SW} (m)**	**Hm_0^{IG}/Hm_0^{SW}**	**Hm_0^{SW}/h**
3	0.68	0.11	0.18	0.60	0.23
2	2.27	0.11	0.38	0.29	0.16
1	3.38	0.14	0.89	0.16	0.26
ADCP	11.6	-	0.74	-	-
TIDE 4 (high-tide)					
PT No.	**h (m)**	**Hm_0^{IG} (m)**	**Hm_0^{SW} (m)**	**Hm_0^{IG}/Hm_0^{SW}**	**Hm_0^{SW}/h**
3	4.00	0.09	0.68	0.13	0.17
2	5.55	0.10	0.67	0.15	0.12
1	6.82	0.08	0.72	0.12	0.11
ADCP	14.9	-	0.68	-	-

3.2. *Infragravity wave propagation*

Table 1 and Figure 2 describe the general IG wave hydrodynamics but they are not sufficient to understand the frequency evolution of the IG wave field. Therefore, the wave spectra of the IG and SW wave band were computed and shown in Figure 3. Regarding the spectrum evolution during low tide (Figure 3a)), the peak frequency (f_p) was approximately 0.083 Hz and the spectral energy density (SED) associated to the f_p

decreased shorewards. This was representative of SW dissipation across the surf zone. The frequency peak of 0.166 Hz at PT1 also agrees with the first superharmonic (2 f_p).

During high-tide there was only small dissipation around the f_p of 0.083 Hz between PT1 and PT3 (Figure 3b)). This is consistent with wave shoaling up to the point of wave breaking. It was also clearly observed the first and second superharmonics of 0.166 and 0.249 Hz (2 f_p and 3 f_p). These observations are in close relation to the ones reported, for example, by Herbers et al. (2000).

Regarding IG waves and during low-tide, the most offshore sensor displayed two frequency peaks at 0.015 and 0.025 Hz (Figure 3a) thick blue line). Shoreward, at PT2, these peaks become well defined around the same frequencies (Figure 3 – a) dashed red line). Very close to the shore, at PT3, the 0.025 Hz peak increased and the 0.015 Hz peak shifted to an even lower frequency centered close to 0.01 Hz (Figure 3 – a) dashed-dot black line). During high-tide the behavior was different. The deepest sensor only displayed one clear low-frequency close to 0.01 Hz. The spectra shifts towards a more broad-banded at PT2 and, finally, two peaks are distinguishable for PT3. The first peak was around 0.01 Hz and the second close to 0.035 Hz.

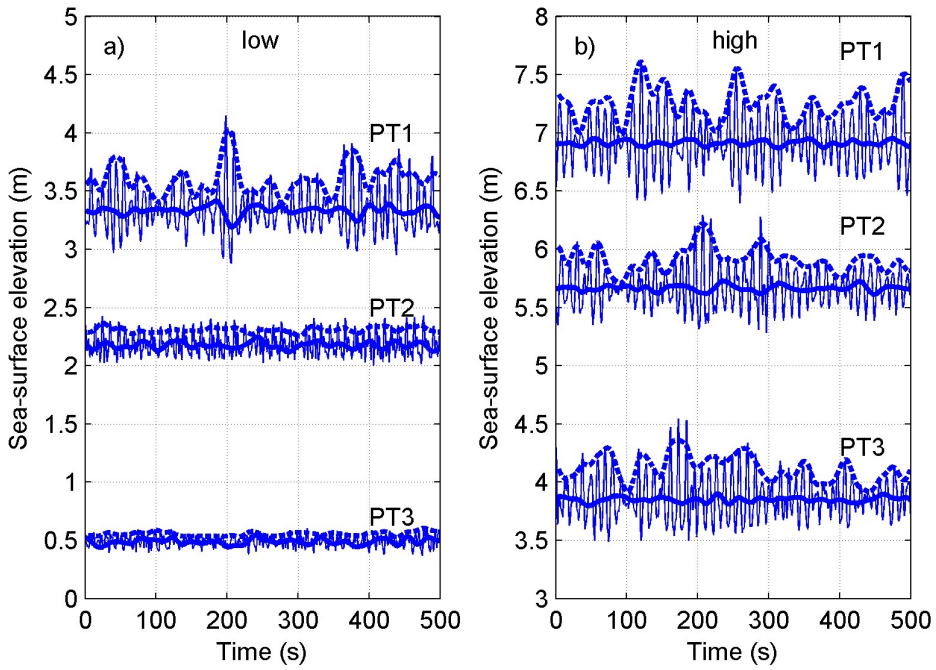

Figure 2 – Time-series of short-wave (thin lines) and infragravity wave (thick lines) sea-surface elevations and short-wave envelope (dashed lines) around the mean water depth for each instrument and for the low- and high-tide a) and b), respectively.

The frequency shift observed during low-tide is expected and may result from non-linear near-resonant interactions between IG and SW (De Bakker et al., 2015) since there was no evidence of energy dissipation for Hm_0^{IG} (Table 1). Two IG wave frequencies may interact with each other and might transfer energy to other IG wave frequency. For example, the interaction between 0.01 and 0.012 Hz will transfer energy to 0.022 Hz through near-resonant non-linear energy transfer mechanism.

However, the frequency of 0.035 Hz is hardly explained especially if one compares the PT3 at low-tide with PT1 during high-tide which were approximately at the same water depths (Table 1).

Two different behaviors were detected regarding the previous analysis and two different regimes can be identified over the IG band. A low-frequency band between 0.005 to 0.02 Hz which experienced frequency shifts to lower frequencies. A high-frequency band between 0.02 to 0.04 Hz which displayed an energy grow shorewards. This separation in two IG wave bands with different behaviors is similar with other studies (e.g.

Fiedler et al., 2015).

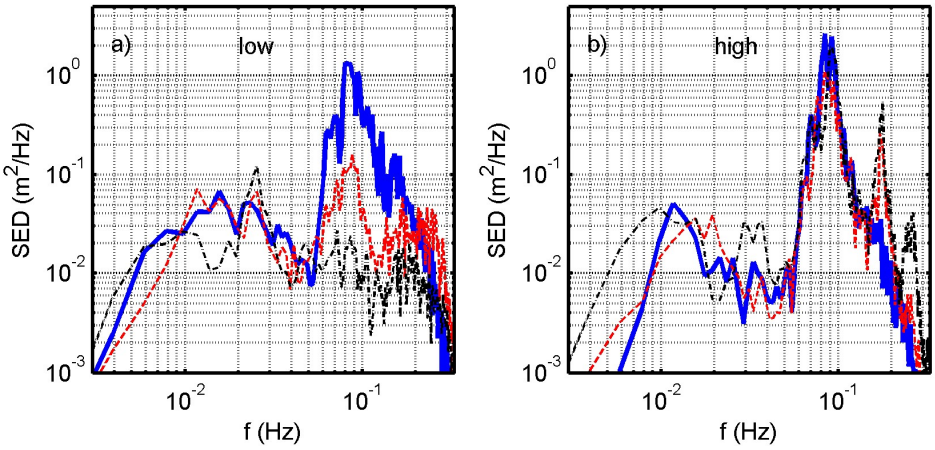

Figure 3 – Infragravity wave band spectrum for PT1 (solid blue lines), PT2 (dashed red lines) and PT3 (dashed-dot black line) during: a) low-tide, and b) high-tide.

3.3. *Infragravity wave generation*

The generation of IG wave energy is addressed in this section. Similar to other authors, the cross-correlation between the SW envelope and the IG sea-surface elevation was calculated at the location of each PT both for low- and high-tide (Figure 4). During low-tide, at PT1 there was a negative correlation for a time lag of approximately 5 s (Figure 5 – a) thick blue line).

Further shoreward, at PT2, the correlation weakens and a negative value is seen at a lag of 18 s. Near the shore, at PT3, it seems that the SW envelope is forcing the IG wave because the positive correlation for a time lag of 5 s is in agreement with the breakpoint mechanism.

During high-tide, the correlations for a time lag close to 0 s were negative both for PT1 and PT2. Shorewards, at PT3, there was in fact a significant negative correlation value for a small time lag (~5 s) but also another, and stronger, at a time lag of 35 s.

During low-tide, these results showed an evidence of the bound wave generation mechanism in a similar way reported by other authors (e.g. Masselink, 1995). Close to the shoreline, the positive peak seems to indicate the breaking point mechanism but this can be highly debatable when looking to Figure 2 – a). For such shallower depths, the SW envelope no longer exists because the wave groups were destroyed during breaking. During high-tide, the same evidences can be detected at PT1 and PT2 regarding the bound-wave mechanism.

The pattern observed for PT3 during high-tide was more intriguing. We tried to understand if these peaks were related to the time lag that a free wave generated at PT3 takes to propagate shorewards, reflects at the shoreline and reach the PT3 position. Considering a total distance of 120 m and a wave celerity equals to 6.3 m/s (h = 4 m) the time interval should be 20 s. Therefore, no explanation was found to support these results.

The cross-correlation between the SW envelope at PT3 and the IG sea-surface elevation at each PT was also computed and shown in Figure 5. During low-tide, it was observed a negative correlation value of -0.05 for a time lag of approximately 4 s at PT2 and another negative value close to -0.1 for a lag of 18 s at PT3. This negative correlation values can be an evidence that the SW envelope at PT1 is still correlated with the IG sea-surface elevation at PT2 and PT3. During high-tide the behavior was different. It was observed that at PT2 there was a negative correlation value of -0.07 for a time lag of 30 s. At PT3, all the correlation values are within the 95% confidence limits and there is no correlation. This last evidence implies that the IG wave at PT3 is no longer forced by the SW envelope at PT1.

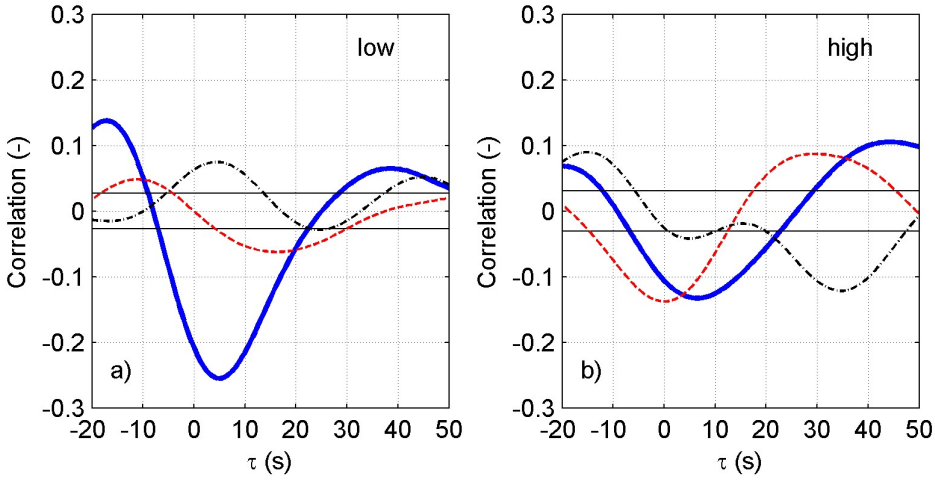

Figure 4 – Cross-correlation between the short-wave envelope and the infragravity wave elevation for PT1 (thick blue lines), PT2 (dashed red lines) and PT3 (dashed-dot black line) during low- and high-tide a) and b), respectively. Thin black lines represent the 95% confidence intervals of the cross-correlation estimates.

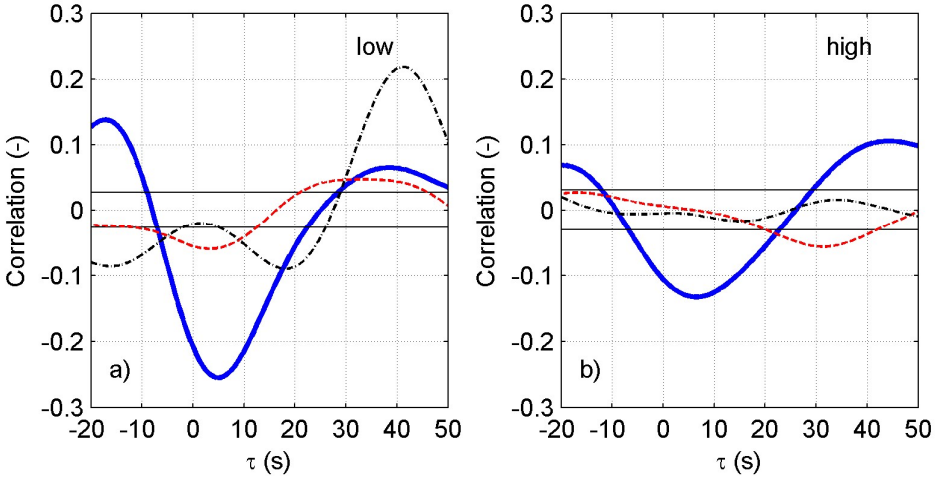

Figure 5 – Cross-correlation between the short-wave envelope at PT3 and the infragravity wave elevation at PT1 (thick blue lines), PT2 (dashed red lines) and PT3 (dashed-dot black line) during low- and high-tide a) and b), respectively. Thin black lines represent the 95% confidence intervals of the cross-correlation estimates.

3.4. *Infragravity wave phase evolution*

In order to better understand the infragravity wave phase evolution, the cross-spectra between the SW envelope and the IG elevation were computed both for low- and high-tide (Figure 6). The absolute value of the cross-spectra for each PT was computed to understand if there was in fact some energy present at that frequency (Figure 6 – left panels). The phase lag evolution of the IG elevation behind the SW envelope (Figure 6 – right panels) was also computed.

The evolution presented at Figure 6 – b) is very similar to the one presented by several authors (e.g. Battjes et al., 2004). The IG wave starts to lag behind the SW envelope and this increases shorewards. Also, the

frequencies between 0.02 and 0.04 Hz increased more than the frequencies between 0.005 and 0.02 Hz. These evidences further supports the different characteristics of two IG wave bands. At high-tide, considerable scatter occurred and the results are difficult to interpret. Besides, the majority of the phase lags were between 0 and 0.5 and this is consistent with the expected lags that would occur before the breaking region.

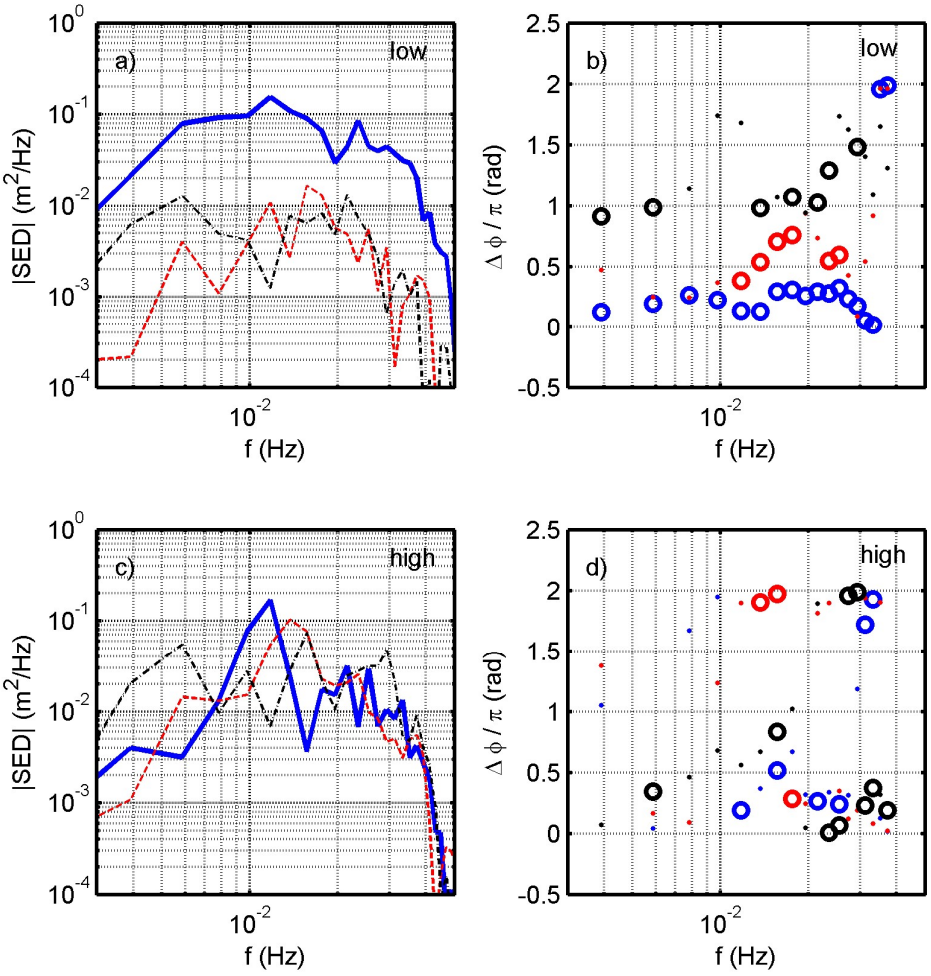

Figure 6 – Cross-spectrum between the short-wave envelope and the infragravity wave elevation for PT1 (thick blue lines), PT2 (dashed red lines) and PT3 (dashed-dot black line) during low- and high-tide a) and c), respectively. Phase lag between the short-wave envelope and the infragravity wave elevation for PT1 (blue), PT2 (red) and PT3 (black) during low- and high-tide b) and d), respectively. Circles stands for values where the squared coherence was greater than 0.35 and dots for values where it was lower.

Finally, the cross-spectra between the SW envelope at PT3 and the IG sea-surface elevation at each PT was also computed (Figure 7). During low-tide, the phase-evolution rapidly increases for frequencies above 0.02 Hz at PT1. This evidence is again consistent with the different behavior between the two IG wave bands. Moreover, the vast majority of the coherence values at PT2 were not significant at 95% confidence level which might indicate that the two signals are not correlated and this is in agreement with the small values of the correlation coefficient between the SW envelope at PT3 and the IG sea-surface elevation at PT2 (Figure 5 – a)). Regarding high-tide, the scatter presented in the phase-evolution (Figure 7 – d)) did not allow any interpretation of the results.

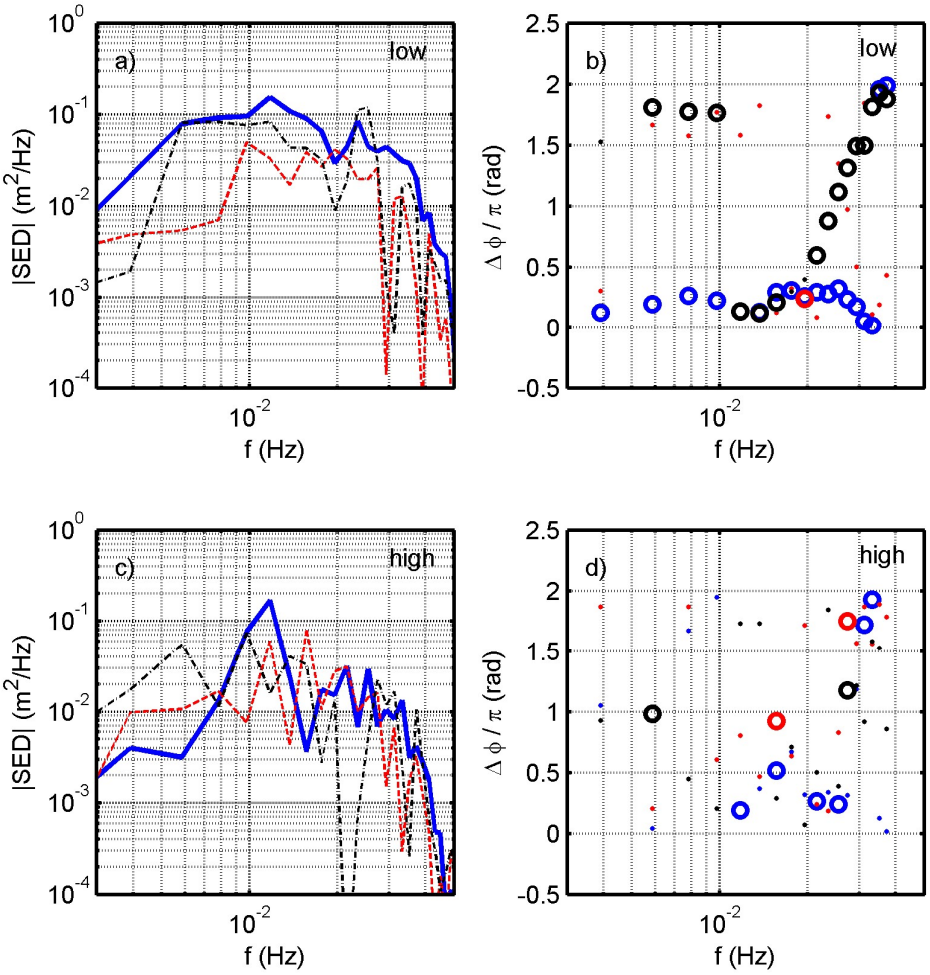

Figure 7 – Cross-spectrum between the short-wave envelope at PT3 and the infragravity wave elevation at PT1 (thick blue lines), PT2 (dashed red lines) and PT3 (dashed-dot black line) during low- and high-tide a) and c), respectively. Phase lag between the short-wave envelope at PT3 and the infragravity wave elevation at PT1 (blue), PT2 (red) and PT3 (black) during low- and high-tide b) and d), respectively. Circles stands for values where the squared coherence was greater than 0.35 and dots for values where it was lower.

4. Conclusions

Field data presented in this study depart from other field studies because these data were obtained in an embayed beach. The IG wave energy increased shoreward during low-tides and remained similar during high-tides. Two different IG wave bands were identified: from 0.005 to 0.02 Hz and from 0.02 to 0.04 Hz. The cross-shore spectral evolution during low-tide supports the near-resonant non-linear energy transfer mechanism between IG wave frequencies. Two lower IG wave frequencies interact with each other and energy is transferred to the higher IG wave frequency. The value of this high IG wave frequency corresponds to the sum between the two low IG wave frequencies.

IG wave generation was greatly explained by the bound wave theory because a strong negative correlation occurred between the SW envelope and the IG wave elevation for a time lag of approximately 5 s. The phase-lag evolution between the SW envelope and the IG wave elevation increased shoreward and was frequency-dependent consistent with previous observations.

Acknowledgements

The authors would like to acknowledge all the participants in the field experiment. Project RAIA.CO (0520_RAIA_CO_1_E), Observatório Marinho da Margem Ibérica e Litoral, funded by the European Fund for Regional Development (EFDR) through the Programa Operacional de Cooperação Transfonteiriça Espanha-Portugal (POCTEC) has funded the field experiment. The first author acknowledges a PhD fellowship granted by Fundação para a Ciência e Tecnologia (grant PD/BD/114463/2016).

References

Aagaard, T. (1990). Infragravity waves and nearshore bars in protected, storm-dominated coastal environments. *Marine Geology*, 94(3): 181-203.

Baldock, T. E., and Huntley, D. A. (2002). Long–wave forcing by the breaking of random gravity waves on a beach. *Proceedings of the Royal Society London, Series A*, 458(2025): 2177-2201.

Battjes, J. A., Bakkenes, H. J., Janssen, T. T., and Van Dongeren, A. R. (2004). Shoaling of subharmonic gravity waves. *Journal of Geophysical Research: Oceans*, 109(C02009).

Bowers, E. C. (1977). Harbour resonance due to set-down beneath wave groups. *Journal of Fluid Mechanics*, 79(01): 71-92.

Castelle, B., and Coco, G. (2012). The morphodynamics of rip channels on embayed beaches. *Continental Shelf Research*, 43: 10-23.

De Bakker, A. T. M., Herbers, T. H. C., Smit, P. B., Tissier, M. F. S., and Ruessink, B. G. (2015). Nonlinear infragravity–wave interactions on a gently sloping laboratory beach. *Journal of Physical Oceanography*, 45(2): 589-605.

De Bakker, A. T. M., Tissier, M., Marieu, V., Sénécha, N., Ruju, A., Lara, J., and Ruessink, G. (2013). Infragravity wave propagation and dissipation on a low-sloping laboratory beach. *In Proceedings of the Coastal Dynamics 2013*: 443-452.

Fiedler, J. W., Brodie, K. L., McNinch, J. E., and Guza, R. T. (2015). Observations of runup and energy flux on a low-slope beach with high-energy, long-period ocean swell. *Geophysical Research Letters*, 42(22): 9933-9941.

Garrett, C., and Petrie, B. (1981). Dynamical aspects of the flow through the Strait of Belle Isle. *Journal of Physical Oceanography*, 11(3), 376-393.

Guza, R. T., and Thornton, E. B. (1985). Observations of surf beat. *Journal of Geophysical Research: Oceans*, 90(C2): 3161-3172.

Henderson, S. M., Guza, R. T., Elgar, S., Herbers, T. H. C., and Bowen, A. J. (2006). Nonlinear generation and loss of infragravity wave energy. *Journal of Geophysical Research: Oceans*, 111(C12007).

Herbers, T. H. C., Russnogle, N. R., and Elgar, S. (2000). Spectral energy balance of breaking waves within the surf zone. *Journal of Physical Oceanography*, 30(11), 2723-2737.

Inch, K., Davidson, M., Masselink, G., and Russel, P. (2015) Propagation and dissipation of infragravity waves on a dissipative beach with energetic wave forcing. *In Proceedings of the Coastal Sediments 2015.*

Inch, K., Davidson, M., Masselink, G., and Russell, P. (2017). Observations of nearshore infragravity wave dynamics under high energy swell and wind-wave conditions. *Continental Shelf Research*, 138: 19-31.

Janssen, T. T., Battjes, J. A., and Van Dongeren, A. R. (2003). Long waves induced by short-wave groups over a sloping bottom. *Journal of Geophysical Research: Oceans*, 108(C8): 1-8.

Longuet-Higgins, M. S., and Stewart, R. W. (1962). Radiation stress and mass transport in gravity waves, with application to 'surf beats'. *Journal of Fluid Mechanics*, 13(4): 481-504.

Loureiro, C., Ferreira, Ó., and Cooper, J. A. G. (2012). Extreme erosion on high-energy embayed beaches: influence of megarips and storm grouping. *Geomorphology*, 139: 155-171.

MacMahan, J. H., Thornton, E. B., and Reniers, A. J. (2006). Rip current review. *Coastal Engineering*, 53(2): 191-208.

Masselink, G. (1995). Group bound long waves as a source of infragravity energy in the surf zone. *Continental Shelf Research*, 15(13): 1525-1547.

Rabinovich, A. B. (2008). Seiches and harbor oscillations. *Handbook of Coastal and Ocean Engineering*, 193-236.

Ruessink, B. G. (1998). The temporal and spatial variability of infragravity energy in a barred nearshore zone. *Continental Shelf Research*, 18(6), 585-605.

Russell, P. E. (1993). Mechanisms for beach erosion during storms. *Continental Shelf Research*, 13(11): 1243-1265.

Short, A. D., and Masselink, G. (1999). Embayed and structurally controlled beaches. *Handbook of Beach and Shoreface Morphodynamics*, 1, 230-249.

Symonds, G., Huntley, D. A., and Bowen, A. J. (1982). Two-dimensional surf beat: Long wave generation by a time-varying breakpoint. *Journal of Geophysical Research: Oceans*, 87(C1): 492-498.